AT622 Section 12
Heating

Figure 12.1 provides a perspective on the topic of radiative heating. For infrared radiation, a layer in the atmosphere emits radiation at a rate defined by its temperature and the emissivity of the layer. This layer also receives radiation from layers above and layers below. When it receives more than it emits, the layer radiatively heats and *vice versa.* We think of this as an exchange process: radiation is exchanged between the reference layer and the surrounding atmosphere and surface. The aim of this section is to consider the dominant exchanges and how they shape the radiative heating distribution in the atmosphere.

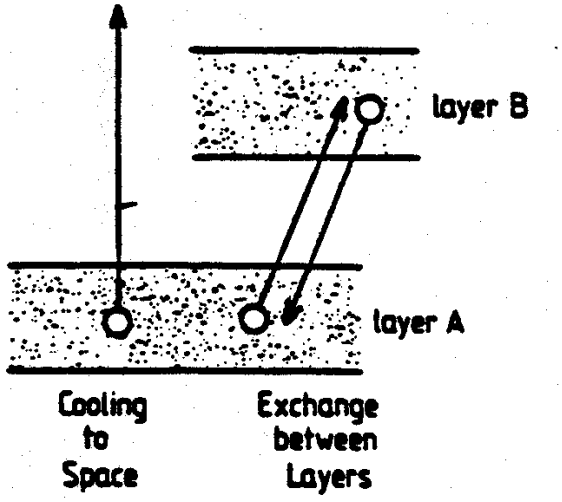

Fig. 12.1 A schematic of two different contributions to the radiative cooling by a layer. The first is by cooling to space (this occurs mainly in the transparent regions of the absorption spectrum in which contributions by surrounding layers are small). The second is by mutual exchange between layers; such as illustrated between layer A (reference) and layer B.

12.1 The Radiative Heating Rate

Consider a volume of atmosphere irradiated by a flux $F_x - \frac{\partial F_x}{\partial x}\delta x/2$ on one face and a flux $F_x + \frac{\partial F_x}{\partial x}\delta x/2$ exiting on the other face (Fig. 12.2). The net flow of energy into the volume along x is

$$net = -\frac{\partial F_x}{\partial x}\delta x \delta y \delta z$$

In three dimensions, the rate at which heat is added per unit volume of air is

$$\dot{Q} = -\nabla \cdot F = -\left[\frac{\partial F_x}{\partial x} + \frac{\partial F_y}{\partial y} + \frac{\partial F_z}{\partial z}\right] \cdot \delta V. \qquad (12.1)$$

For monochromatic, radiative equilibrium

$$\nabla \cdot F_\lambda = 0$$

where the wavelength dependence of the flux is brought to view.

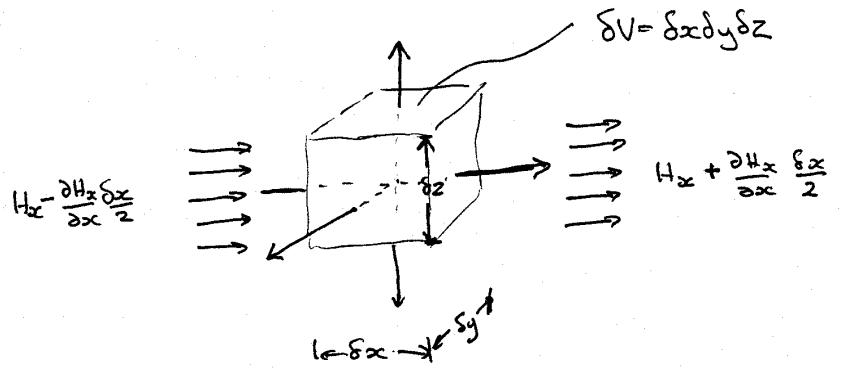

Fig. 12.2 Energy budget of a volume of atmosphere used to establish the heating rate equation.

From the first law of thermodynamics, the heat added to a volume per unit mass is

$$Q = C_p dT - V dp$$

from which it follows

$$\dot{Q} = C_p \frac{dT}{dt} - V \frac{dp}{dt} \tag{12.2}$$

Combining Eqns. (12.1) and (12.2), we obtain

$$C_p \frac{dT}{dt} = -(\nabla \cdot F)\delta V \approx -\frac{dF_{net}}{dz} \cdot \delta V \tag{12.3}$$

And, using the specific heat $c_p = \frac{C_p}{m}$ and assuming that heat is added at constant pressure, we derive

$$\frac{dT}{dt} = -\frac{1}{\rho c_p}\frac{dF_{net}}{dz} \tag{12.4a}$$

or for an atmosphere in hydrostatic equilibrium,

$$\frac{dT}{dt} = \frac{g}{c_p}\frac{dF_{net}}{dp} \tag{12.4b}$$

for a plane parallel atmosphere (for which x and y variability is neglected). This is the radiative heating rate and defines the **potential** of radiation for heating or cooling the atmosphere.

Heat added at constant temperature (e.g., tropics)

$$\frac{dz}{dt} = -\frac{1}{\rho g}\nabla \cdot F \approx \frac{1}{\rho g}\frac{dF}{dz} \tag{12.4c}$$

or

$$\frac{dz}{dt} = -\frac{dF_{net}}{dp} \tag{12.4d}$$

which defines the **potential** of radiation for inducing vertical motion.

Example 12.1: The heating rate of the atmosphere

Based on Fig. 6.13, we deduce that

$$\frac{dF_{net}}{dp} \approx \frac{-100}{1013\times 100}$$

in which case it follows that

$$\frac{dT}{dt} = \frac{g}{c_p}\frac{dF_{net}}{dp} \approx -\frac{9.8}{1004}\times\frac{100}{1013\times 100}\times 86400 = -0.83 \text{ Kday}^{-1}$$

or alternatively that

$$\frac{dz}{dt} = \frac{dF_{net}}{dp} = -\frac{-100}{1013\times 100}\times 86400 = -85 \text{ mday}^{-1}$$

12.2 The IR Radiative Heating From Satellites

The rate of cooling of the atmospheric column follows from Eqn. (12.4b) as

$$\frac{dT}{dt} = -\frac{g}{c_p p_s}\Delta F_{net} \tag{12.5}$$

where the flux difference

$$\Delta F_{net} = -(\sigma T_s^4 - F_\infty - F_g)$$

which can be written as

$$\Delta F_{net} = -F_{\infty}\left(\frac{\sigma T_s^4}{F_{\infty}} - \frac{F_g}{F_{\infty}} - 1\right)$$

the column heating becomes

$$\frac{dT}{dt} = \frac{gF_{\infty}}{c_p p_s}[\mathcal{G} - \mathcal{F} - 1], \tag{12.6}$$

where we introduce the ratio terms defined earlier in Eqns. (6.5) and (11.7) and which vary in a systematic way with the PWC *w*. Furthermore, for a given *w*, the heating of the column varies proportionally with the clear-sky outgoing longwave radiation F_{∞}.

Using the retrieval strategy to estimate clear-sky values of F_g from satellite measurements of F_{∞} and *w* as described earlier and substituting a value of 1013 mb for p_s and use the monthly mean SST of Reynolds for T_s in Eqn. (12.6), we arrive at monthly mean distributions of the column averaged clear-sky heating rates shown in Figs. 12.3a and b (negative values represent cooling) for July 1988 and January 1989, respectively. A reasonable estimate of the uncertainty of the monthly averaged values of F_{∞} and F_g is ±10 Wm^{-2} based on published estimates in ERBE clear-sky flux uncertainties and in the uncertainties in F_g expressed by the rms differences discussed in relation to the comparisons shown previously in Fig. 10.8. These flux uncertainties in turn imply an uncertainty of approximately ±0.2 K/day in the column cooling rate. The SSM/I fields of *w* for July 1988 and January 1989, which are used to produce these heating rate distributions, are also shown in Figs. 12.3c and d for comparison. It is evident that the clear sky column heating rate distributions resemble the distributions of *w*, which is consistent with Eqn. (12.6) and the relationship between $\mathcal{G}$, $\mathcal{F}$ and *w*. The largest coolings occur in the moist equatorial regions and in the areas of moisture convergence over the northwest Pacific and Atlantic Oceans during July as well as in the South Pacific Convergence Zone.

The association between the column averaged heating rate and *w* is explored further in Figs. 12.4a and b, where the data displayed in Fig. 12.3a and c and Figs. 12.3b and d, respectively, are plotted against each other. Based on Eqn. (12.6) and the relationships assumed between the ratio quantities and *w*, we expect the cooling rate to increase in an approximate linear way with increasing *w* as confirmed in Figs. 12.4a and b. Linear fits of both $\mathcal{F}$ and $\mathcal{G}$ as a function of *w* yield the following slope coefficients: c_2 = 0.01015 $(kgm^{-2})^{-1}$ and c_1 = 0.00524 $(kgm^{-2})^{-1}$, respectively, which, according to Eqn. (12.6), implies a slope of -0.005 $(kgm^{-2})^{-1}$. An example of a relationship with this slope, defined using the global-mean value F_{∞} = 266 Wm^{-2}, is also given on each diagram for reference. The column cooling rate deviates from this simple linear dependence on *w* in such a way that the rate of increase of column cooling with increasing *w* above about 40 kgm^{-2} decreases.

When the column cooling rate is expressed as a function of SST rather than as a function of *w* as it is shown in Figs. 12.4c and d, a number of features emerge. The first is the general change in the cooling-SST slope for SST exceeding approximately 295 K due to the rapid increase in *w* as the SST increases beyond this value. The second feature that emerges from Figs. 12.4c and d are the winter-summer hemispheric branches in the column cooling similar to those noted in the $\mathcal{G}$-SST relationship. The characteristics of the relation between the column cooling rate and SST, especially the increased rate of cooling with increasing SST, may be better understood by reference to Fig. 12.5. This

diagram presents scatter diagrams of fluxes as a function of SST. The left panels are F_∞ and F_g derived from satellite data for July 1988 (left panels) as a function of SST and the matching fluxes derived from SAMSON are shown to the right. We can deduce that the enhanced rate of change of cooling for SSTs greater than about 295 K is a result of the enhanced emission from the atmosphere to the surface associated with the increasing water vapor with SST at these temperatures. The rate of increase of emission from the atmosphere as the SST increases exceeds the rate of change of the emission from the surface (i.e., σT_s^4). The latter is represented by the solid curve in the lower two panels of Fig. 12.4. For the SST > 290 K, we deduce that $\Delta F_g/\Delta \mathrm{SST} \approx 15$ Wm^{-2} K^{-1} and that $\Delta \sigma T_s^4 / \Delta \mathrm{SST} \approx$ Wm^{-2} K^{-1}.

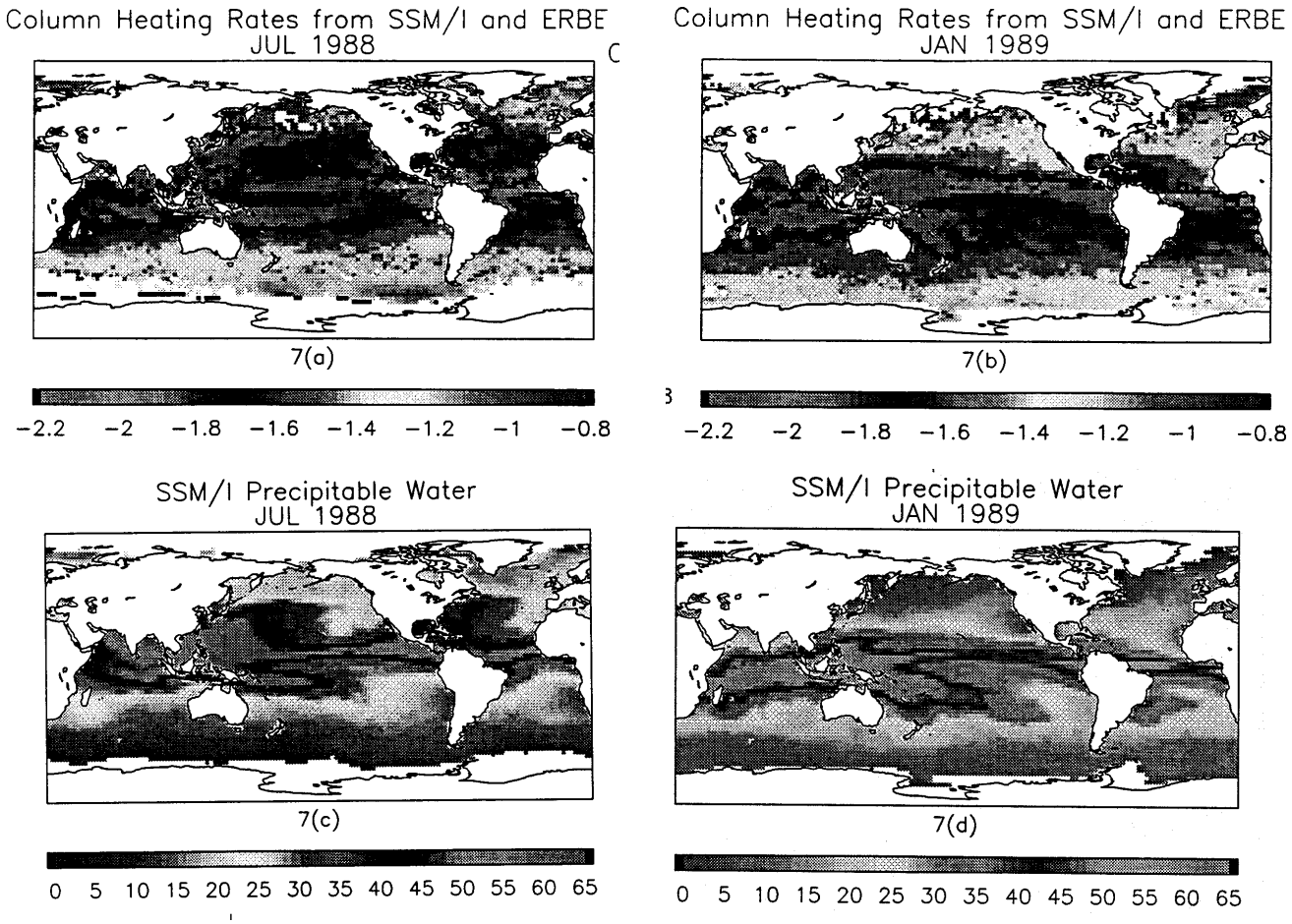

Fig. 12.3 (a) and (b) clear-sky column cooling rate distributions for July 1988 and January 1989 (in units of Kday^{-1}). (c) and (d) same as (a) and (b) except for vertically integrated water vapor (in units of kgm^{-2}).

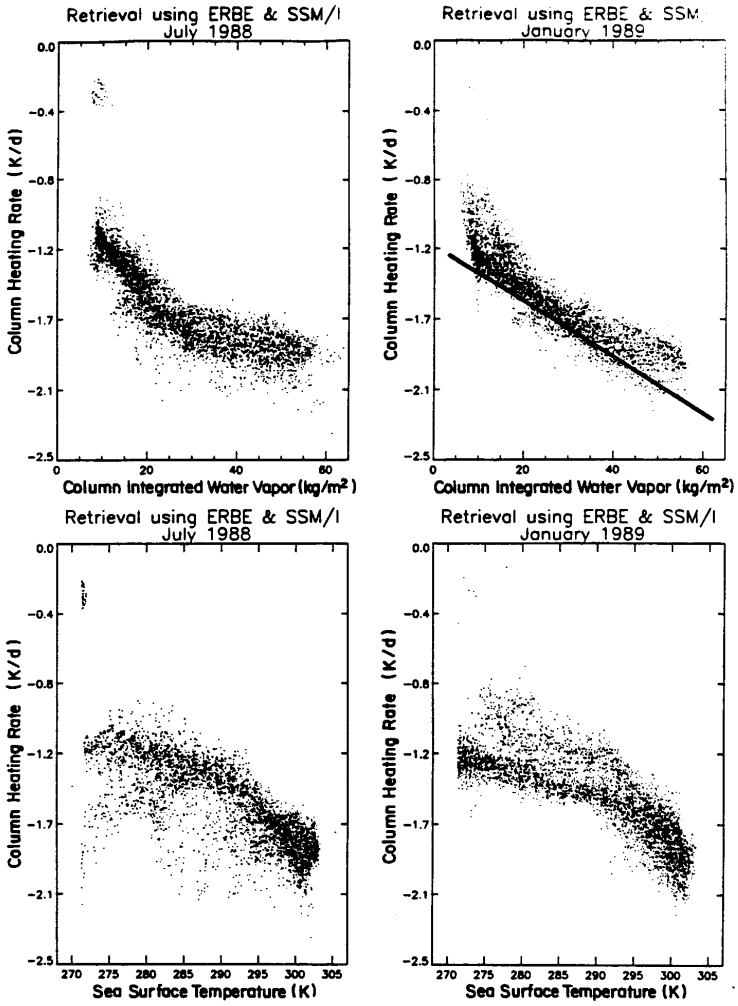

Fig. 12.4 The clear-sky column cooling rate correlated with the SSM/I derived column water vapor obtained from the data of (a) July 1988 and (b) January 1989. The solid lines are simple linear relationships implied by Eqn. (12.6), Fig. 1.3(a) and (b) and F_∞ = 266 Wm^{-2}. The clear-sky column cooling rate correlated with SST for (c) July 1988 and (d) January 1989.

12.3 The IR Radiative Heating Rate Exchange Equation

We start with the flux Eqns. (11.2) written as

$$F_i^+(z) = F_i^+(z=0)T_i^f(0,z) + \int_0^z \pi B_i(z')\frac{dT_i^f}{dz'}(z',z)dz'$$
$$F_i^-(z) = \int_z^\infty \pi B_i(z')\frac{dT^f}{dz'}(z,z')dz' \qquad (12.7)$$

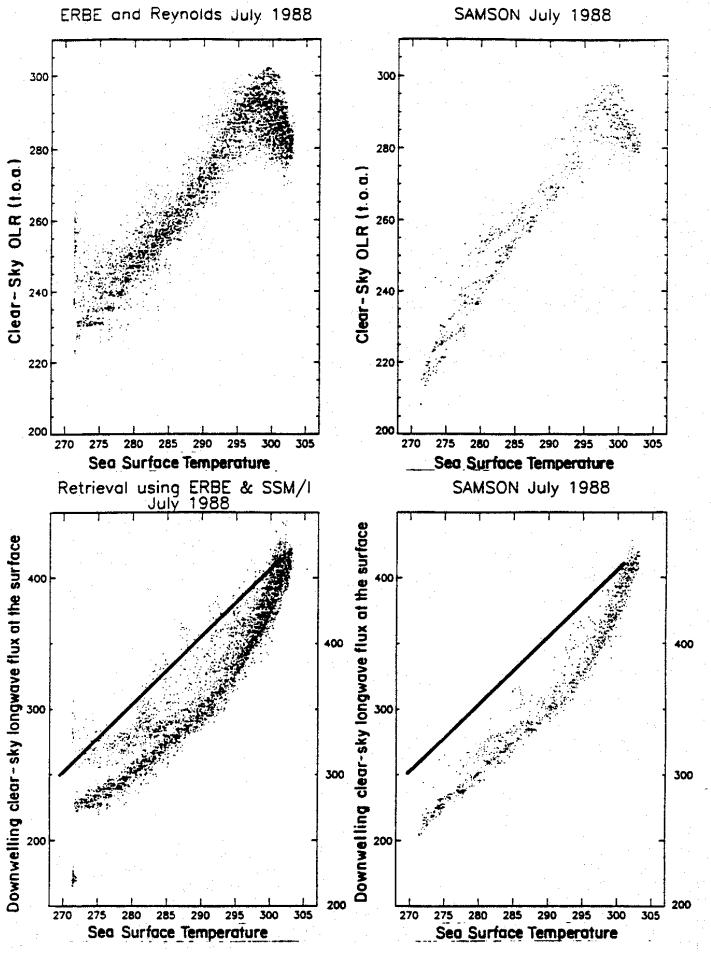

Fig. 12.5 *F_∞ as a function of SST (upper two panels) from ERBE (left) and SAMSON (right). F_g as a function of SST (bottom panels) derived from the retrieval method described in the text (left) and from SAMSON (right). The solid line on each of the bottom panels represents black body emission at the prescribed value of the SST and the scale on the left represents the scale of this blackbody flux.*

for the i^{th} spectral interval. The heating rate for this interval at level z is

$$h_i(z) = \frac{dT}{dt} = -\frac{1}{\rho c_p}\frac{dF_{net,i}}{dz}(z) \tag{12.8}$$

where the net flux at this level is

$$F_{net,i}(z) = F_i^+(z) - F_i^-(z). \tag{12.9}$$

Combining the above into Eqn. (12.8) and differentiating w.r.t. z yields

$$h_i(z) = -\frac{1}{\rho C_p}\left[\left[\pi B_i(0)\frac{d\mathcal{T}_i^f}{dz}(0,z) + \int_0^z \pi B_i(z')\frac{\partial^2 \mathcal{T}_i^f}{\partial z \partial z'}(z,z')dz' + \int_z^\infty \pi B_i(z')\frac{\partial^2 \mathcal{T}_i^f}{\partial z \partial z'}(z,z')dz'\right]\right. \tag{12.10}$$

where we suppose the surface emits as a blackbody such that $F_i^+(z=0) = \pi B(0)$. If we note that

$$\int_0^z \pi B\ (z')\frac{\partial^2 \mathcal{T}_i^f}{\partial z \partial z'}(z,z')dz' + \pi B(z)\frac{d\mathcal{T}_i^f}{dz}(z,0) = 0$$

and

$$\int_z^\infty \pi B_i(z')\frac{\partial^2 \mathcal{T}_i^f}{\partial z \partial z'}(z,z')dz' + \pi B(z)\frac{d\mathcal{T}_i^f}{dz}(z,\infty) = 0$$

then we can add each to Eqn. (12.10) to obtain

$$h_i(z) = \frac{1}{\rho C_p}\left[\begin{array}{l} \underbrace{-\pi B(z)\frac{d\mathcal{T}_i^f}{dz}(z,\infty)}_{A} \underbrace{-\pi[B_i(0)-B(z)]\frac{d\mathcal{T}_i^f}{dz}(z,0)}_{B} \\ \underbrace{-\pi\int_0^z [B_i(z')-B_i(z)]\frac{\partial^2 \mathcal{T}_i^f}{\partial z \partial z'}(z,z')dz'}_{C} \underbrace{-\pi\int_z^\infty [B_i(z')-B_i(z)]\frac{\partial^2 \mathcal{T}_i^f}{\partial z \partial z'}(z,z')dz'}_{D} \end{array}\right] \quad (12.11)$$

TERM A: is the exchange with z and space. Since $\frac{d\mathcal{T}_i^f}{dz}(z,\infty) > 0$, Term A < 0 and this term contributes to cooling at z. This is referred to as the cooling to "space" term and generally the most dominant term in the heating rate equation (Fig. 12.6b). It represents radiation escaping to space primarily through the more transparent regions of the spectrum at lower levels and through the more opaque spectral regions at higher levels. This is discussed in more detail below.

TERM B: this represents the exchange with the underlying surface. Since $B(0) > B(z)$ generally and since $\frac{d\mathcal{T}_i^f}{dz}(z,0) < 0$, this term is positive and contributes to **heating** at z.

TERM C+D: these represent the exchanges with the layers below z (C) and above z (D). For both terms $\frac{\partial^2 \mathcal{T}_i^f}{\partial z \partial z'}(z,z') < 0$ [1]so that these terms define a heating whenever $B(z') > B(z)$. This is usually the case for term C as z' refers to levels below z and thus are typically at a higher temperature. Since z' is above z in term D, this term usually contributes to cooling.

[1]It is relatively simple to demonstrate this. Suppose the transmission function has the form

$$\mathcal{T}_i^f(z,z') = \exp[-k(z-z')]$$

then it trivially follows that

$$\frac{\partial^2 \mathcal{T}_i^f}{\partial z \partial z'}(z,z') = -k^2 e^{-k(z-z')} < 0$$

since $k > 0$.

Figure 12.6a presents an example of the IR cooling rate profile from a radiative transfer model. This diagram shows the contribution to the net cooling by different spectral regions. In general, the troposphere cools at a rate of approximately 2-3 $Cday^{-1}$ primarily through emission by water vapor bands and by the continuum at lower levels although this contribution diminishes rapidly away from the moist tropics. The cooling in the stratosphere is dominated by emission from the 15 μm CO_2 band throughout and by water vapor in the lower stratosphere. Ozone emission gives rise to cooling in the stratosphere (in the vicinity of the ozone layer) and small warming below this. Figure 12.6b presents the profiles of longwave cooling separated into the exchange terms discussed above. The cooling to space term (A) dominates in the troposphere and exchange terms contribute in the stratosphere (B, C and D).

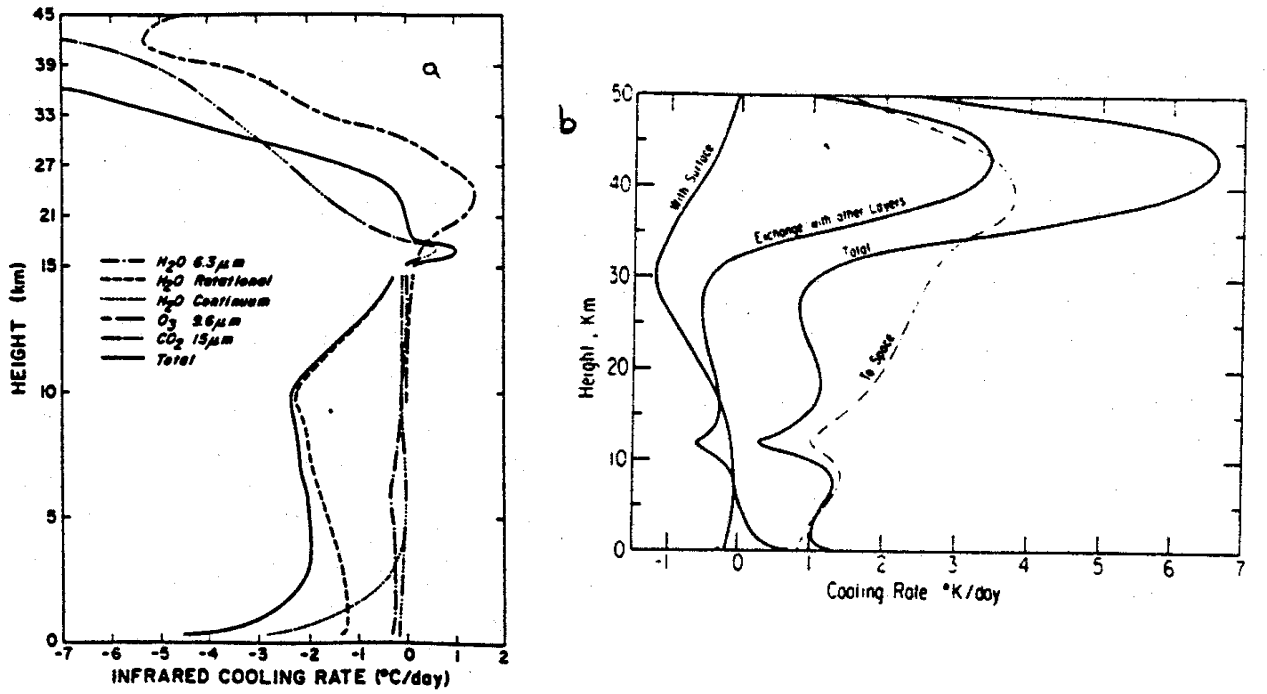

Fig. 12.6 (a) Total and spectral cooling rates in a clear tropical atmosphere (after Foewe and Liou). (b) Contributions of exchanges with surface, space and other layers to the total infrared cooling rate as functions of height.

(a) The Spectral Distribution of Longwave Cooling

The spectral distribution of the infrared cooling rate for selected layers in a model atmosphere is presented in Figs. 12.7a and b. These diagrams indicate how the cooling of layer shifts in its spectral properties from a maximum in the window (continuum absorption) low in atmosphere for the example of a tropical atmosphere shown to the stronger absorption regions of the rotation band higher up. The shaded bar in Fig. 12.7a is the cooling by the layer and the unshaded bars represent the heating of the layer by the surrounding atmosphere. Both this and Fig. 12.7b demonstrate how the net cooling of the layer is the residual of larger exchange terms. A clearer perspective of the spectral contribution to the cooling and how this contribution changes with pressure is presented in Fig. 12.8. The upper panel shows the cooling by a mid-latitude summer atmosphere by water vapor lines alone (no continuum) and the lower panel shows this cooling with the continuum added (both a foreign broadened continuum in the water vapor bands—especially the rotation band and the self broadened *e* continuum in the window). Note how the former enhances the cooling in the upper troposphere and the latter at lower levels.

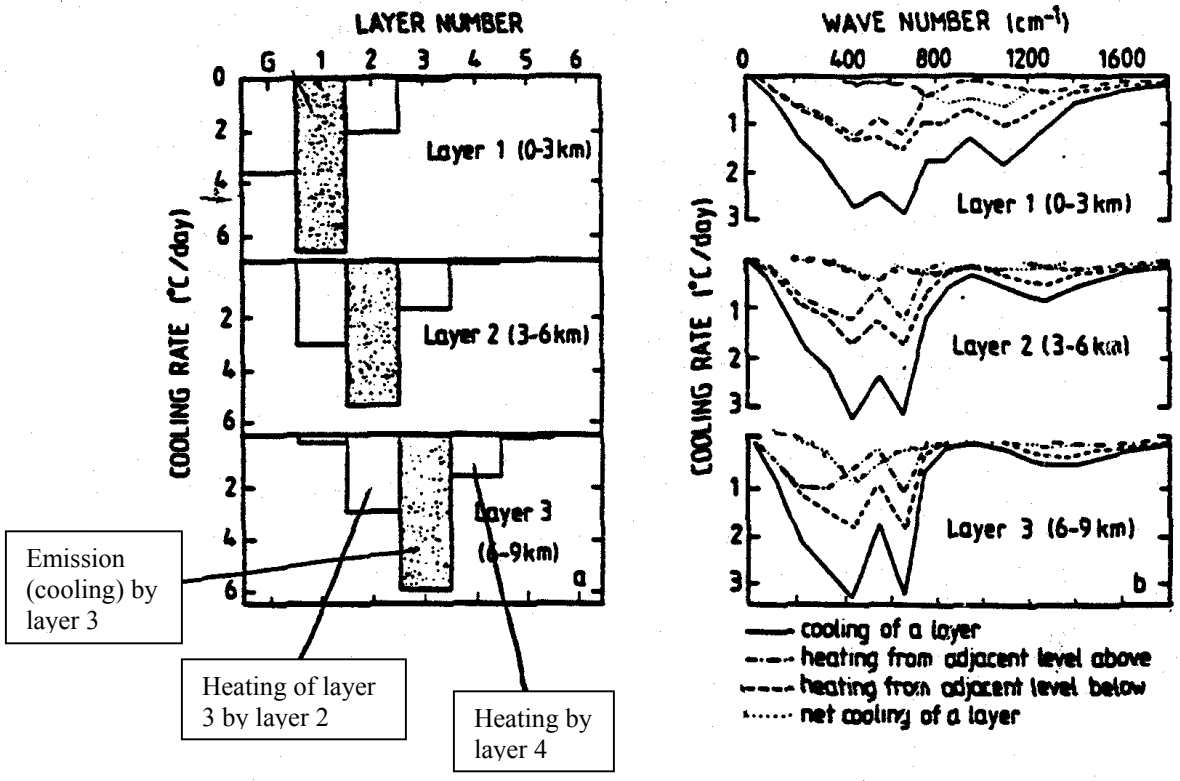

Fig. 12.7 (a) The contribution to the overall radiative cooling by emission from the layer itself (shaded area) and the absorption of radiation that originates from layers adjacent to the reference layer. The separation distance between the reference layer and the surrounding layers is shown on the upper horizontal axis. The total cooling by the reference layer is found from the sum of each individual contribution shown on (a). Note that the shaded area represents cooling, while the open areas define the heating by adjacent layers. (b) The spectral distribution of cooling for the three reference layers shown in (a). The contributions are separated into net cooling of the layer, heating from adjacent layers surrounding the reference layer and heating from all other layers (modified from Wu, 1980).

12.4 Curvature Effects on the IR Cooling

The dominance of the cooling to space term suggest that a convenient approximation to the IR cooling rule

$$\frac{dT}{dt}(z) \to \varepsilon\sigma T^4(z) \quad \text{(local emission at } z\text{)}.$$

However, the situation is more complicated than this as $\frac{dT}{dt}$ depends also in a complicated way on local curvature of temperature and moisture.

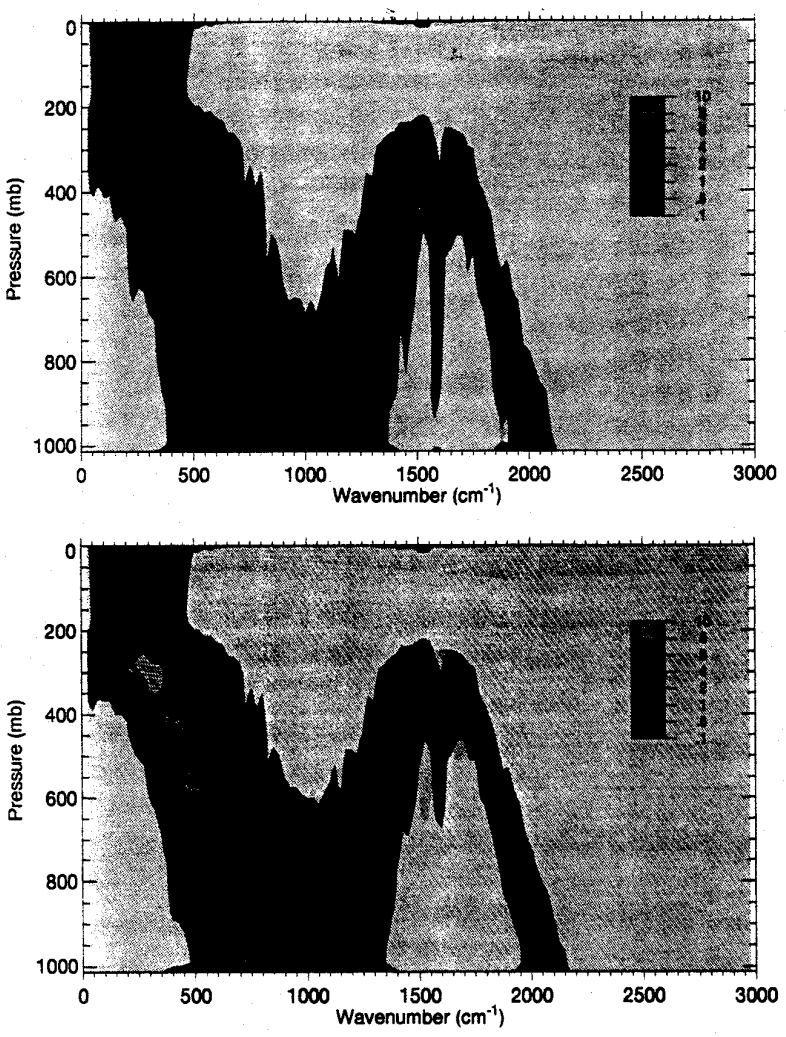

Fig. 12.8 Spectral cooling rate for water vapor for an mls atmosphere. Color scale is in units of Kday^{-1} (cm^{-1})$^{-1}$. The top panel is for no continuum and the bottom panel includes both a p and e continuum.

12.5 Climatology of Radiative Heating

- troposphere generally cools ~ 2° Cday^{-1} except at poles where the smaller water vapor decreased emission
- upper tropical troposphere, lower stratosphere - slight warming
- cooling increases with z in stratosphere.

(a) Solar and Net Heating Rates

We have not discussed solar heating rates in any detail. If we make some (reasonable) assumptions such as neglect Rayleigh scattering and multiple scattering, the clear-sky solar heating can be deduced by treating only absorption of the collimated solar beam, namely

$$F_n(\tau) = F_\odot \underbrace{e^{-\tau/\mu_o}}_{\mathcal{T}_r^f}$$

where we use empirical function for transmission (refer to Section 8). For example, water vapor absorption

$$\mathcal{T}_r^f = 1 - A = 1 - \frac{2.9\tilde{a}}{(1+141.5\tilde{u})^{0.645} + 0.5125\tilde{u}}$$

Scatter indicative of effects

- different absorption data
- different treatment of pressure scaling
- different solar flux data and others.
- O_3 heating increases systematically with z
- troposphere heating ~ 1° Cday^{-1} decreasing to winter pole
- combined heating-minimum in lower stratosphere

(b) Net Heating Rates

An example of the vertical profile of solar heating and IR cooling is shown in Fig. 12.9 derived from a climate model (after Manabe and Strickler, 1964). These profiles can be thought to be representative of globally averaged clear sky conditions. The net (solar+IR) profile highlights the radiative cooling of the troposphere of approximately 1 Kday^{-1} and a stratosphere that is in radiative equilibrium. Here, the solar heating by ozone absorption is balanced largely by CO_2 emission and to a lesser extent by water vapor emission.

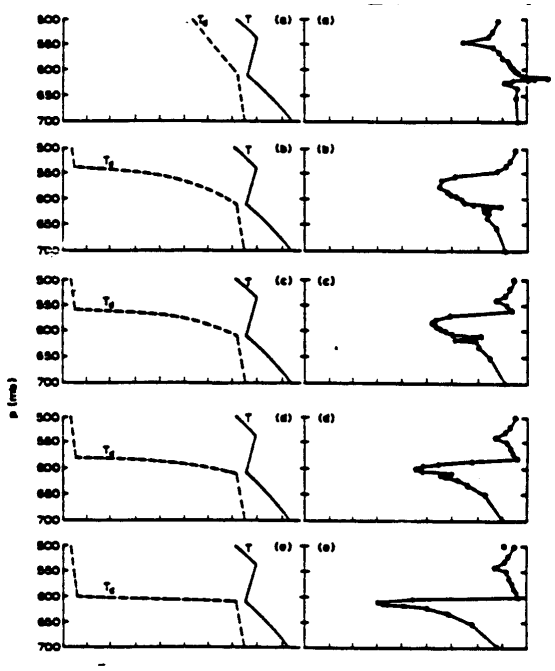

Fig. 12.9 Radiative cooling profiles associated with a temperature inversion and different degrees of "sharpness" in the water vapor profile. T and T_d are the dry and dewpoint temperatures, respectively (after Staley, 1965).

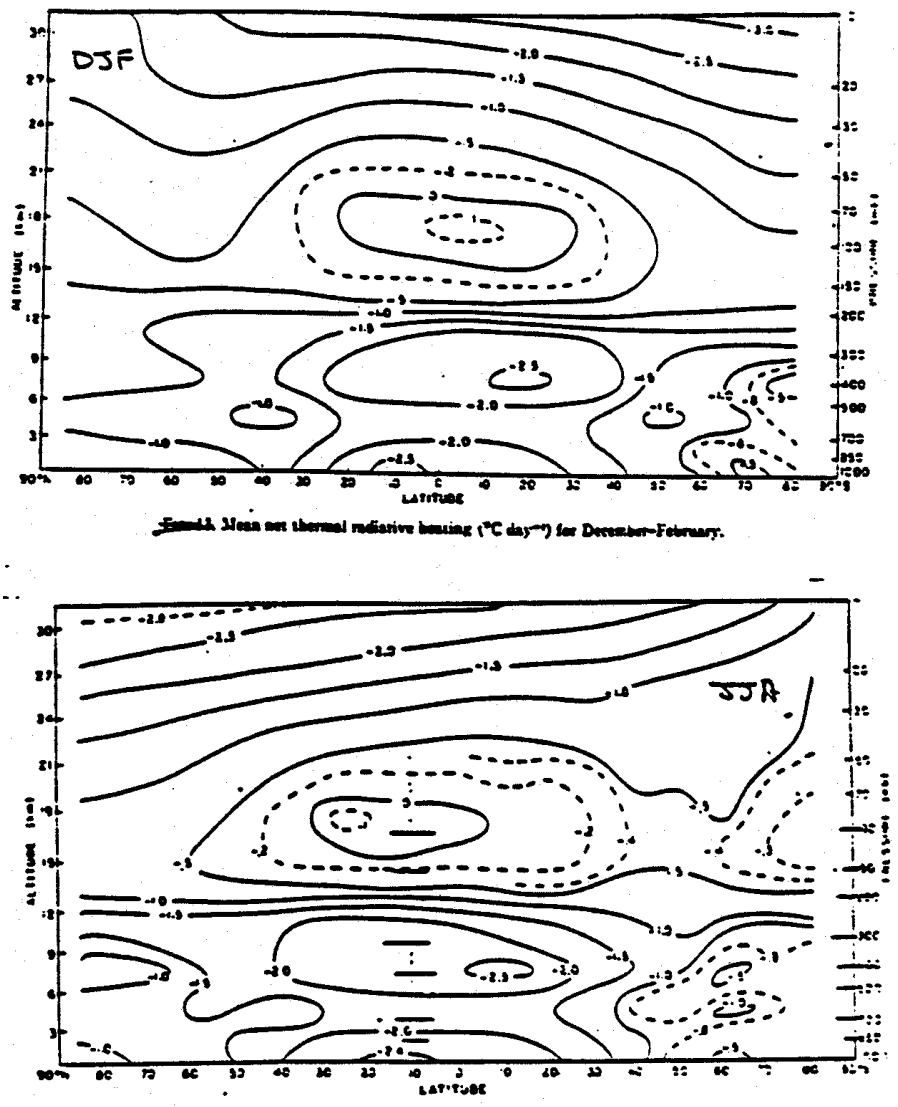

Fig. 12.10 (a) Mean net thermal radiative heating (°Cday^{-1}) for December-February. (b) Mean net thermal radiative heating (°Cday^{-1}) for June-August.

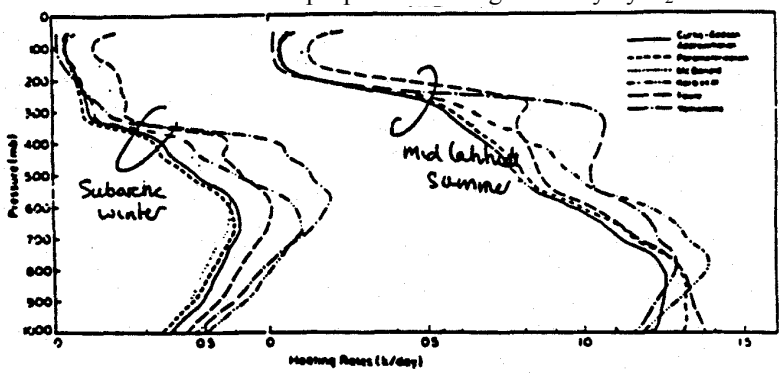

Fig. 12.11 Clear sky solar heating rate profiles due to water vapor absorption in model mid-latitude summer and subarctic winter atmospheres. The profiles were calculated for $\theta_o = 60°$ and $\alpha_g = 0.07$ for a variety of different absorption parameterizations that use either different absorption data and/or different extraterrestrial solar fluxes (refer Table 4 and discussion in text) (from Wang 1976).

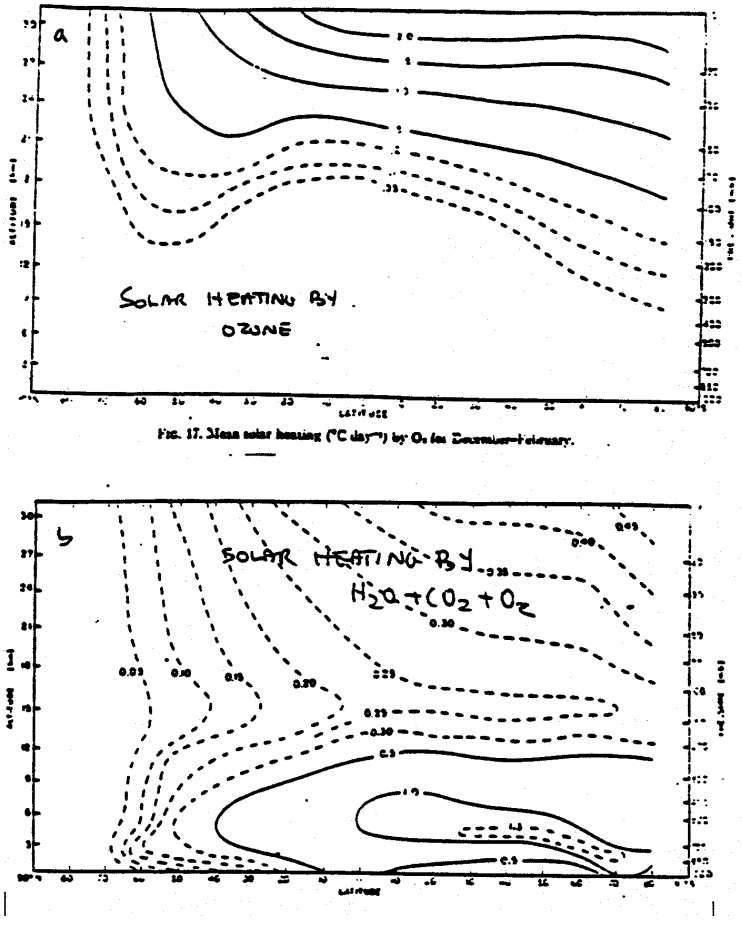

Fig. 12.12 (a) Mean solar heating (°Cday^{-1}) by O_3 for December-February. (b) Mean solar heating (°Cday^{-1}) by $H_2O + CO_2 + O_2$ for December-February.